Technical article

A novel approach to estimate harmonic force excitation for noise diagnosis of electrical machines

***Abstract* — The electromagnetic excited audible noise of electrical machines can be mostly attributed to radial forces on stator toothheads. Classical noise analysis approaches focus then on the wave numbers and frequencies of the spectral decomposition of the air gap field. Numerical approaches on the other hand, make it possible to compute the magnetic field, and thus the force amplitudes, with a much greater accuracy. The approach presented in this paper combines the benefits of both approaches by firstly performing a numerical field analysis, then transforming the radial air gap field into the frequency domain, and finally performing a matrix convolution. The latter operation reveals the relationship between air gap field harmonics and the corresponding force waves acting on the stator teeth. The proposed method is demonstrated on a permanent magnet synchronous machine (PMSM) motor, and numerical results are given. As practical application a brushless DC motor drive and an interior permanent magnet synchronous machine (IPMSM) are analyzed.**

I. Introduction

The reduction of audible noise in electrical machines is attracting more and more attention. Designing low noise electrical machines requires a good understanding of the causes of noise excitation.

Classical analytical approaches for noise analysis in electrical machines rely on the identification of space and time harmonics in the air gap field that generate radial magnetic force waves [1], [2]. The causality relation between force waves and field harmonics can be traced back this way. The drawback of such methods, however, is the limited accuracy of the air gap field and magnetic force wave amplitudes.

Numerical simulations, with e.g. the Finite Element (FE) method, are able to capture finer details and allow an accurate determination of air gap field and magnetic force amplitudes [2], [3] and [4]. Under the standard linear assumption, the vibroacoustic problem is most commonly solved in the frequency domain, either by modal analysis and superposition, or by immediate harmonic analysis. In both cases, the computed electromagnetic force excitations are transformed into the frequency domain. Besides the Fourier transform of time waves, spatial waves are also transformed in order to identify the spatial wave numbers of the air gap field. Comparing the wave numbers and frequencies with those obtained from analytical models, it is possible to identify which magnetic field harmonic predominantly contributes to a given force wave [5].

However, it is not possible by this approach to find out the exact composition of each force wave. The approach presented in this paper overcomes this fundamental drawback by Fourier transforming the magnetic field in time and space directly so as to obtain a representation of the air gap field as a function of wave numbers and frequencies.

The outline of this paper reads as follows: First the analysis of magnetic force waves by means of the analytical model is explained. Afterwards a brief review of the two-dimensional discrete Fourier transform (2D DFT) and the usage of space vectors is given. The subsequent section presents numerical results for one example machine, practical applications and a summary conclude the paper.

II. Generation of magnetic force waves

The air gap field in electrical machines cause force densities on the permeable material of the stator and rotor teeth. Featuring different frequency components, these forces are responsible for mechanical vibrations that radiate air-borne sound.

Magnetic forces acting on a given medium are the divergence of the electromechanical tensor of that medium. Each medium has its own electromechanical tensor, and that of empty space, or air, is the celebrated Maxwell stress tensor [6]. In consequence, magnetic forces come under volume and surface density form. In saturable non-conducting materials, the volume density is basically related with the gradient of the magnetic reluctivity, and it is usually negligible with respect to the surface force density. The latter, located at material discontinuities (e.g. on the stator surface in the air gap), is the divergence in the sense of distribution of the electromechanical tensor. It can be shown [7] that it has a normal component only, whose amplitude is

$$P_r = \left[B_r(H_{1r} - H_{2r}) - (w_1' - w_2')\right], \tag{1}$$

where B_r is the radial magnetic flux density at the interface between the stator and the air gap. H_{1r} and H_{2r} are the radial magnetic field strength in the air and in the stator iron, respectively. The magnetic co-energy density w' is related to the magnetic energy density w by

$$w' = H(B)\cdot B - w(B) = H(B)\cdot B - \int_0^{|B|} |H(x)|dx\,. \tag{2}$$

Due to the constant magnetic permeability of air, w_1' is

$$w_1' = H\cdot B - \frac{1}{2}H\cdot B = \frac{|B|^2}{2\mu_0}\,, \tag{3}$$

where μ_0 denotes the magnetic permeability of vacuum. If the permeability of the iron cannot be considered constant, the magnetic energy term of the iron has to be determined by means of numerical integration along the BH-curve, otherwise, i.e. in the linear case, (1) can be simplified to

$$P_r = \frac{1}{2}\left[B_r(H_{1r} - H_{2r}) - H_t(B_{1t} - B_{2t})\right]. \tag{4}$$

If in addition, the permeability of the iron is sufficiently large and the magnetic field strength in the iron can be neglected, the magnetic force density is finally approximated by

$$P_r = \frac{B_r^2}{2\mu_0}. \tag{5}$$

In steady state operation, the air gap field is periodic in time and space, and it is commonly described by a Fourier series of a

one-dimensional wave by [1]

$$b(x,t) = \sum_{i=0}^{\infty} \hat{B}_i \cos(\nu_i x - \omega_i t - \Psi_i)\,, \tag{6}$$

where ν_i is the wave number, also called "number of pole pairs", and ω_i is the corresponding frequency of one particular wave. Applying (5) gives the force density in the air gap

$$\begin{aligned} p(x,t) \quad &= \frac{1}{2\mu_0}\left[\sum_{j=1}^{\infty} \hat{B}_j \cdot \cos(\nu_j x - \omega_j t - \Psi_j)\right]^2 \\ &= \frac{1}{2\mu_0}\sum_{k=1}^{\infty}\sum_{l=1}^{\infty} \hat{B}_k \hat{B}_l \cdot \cos(\nu_k x - \omega_k t - \Psi_k) \\ &\quad \cdot \cos(\nu_l x - \omega_l t - \Psi_l) \\ &= \frac{1}{2\mu_0}\sum_{k=1}^{\infty}\sum_{l=1}^{\infty} \frac{\hat{B}_k \hat{B}_l}{2} \\ &\quad \cdot \cos((\nu_l \pm \nu_k)x - (\omega_l \pm \omega_k)t - \Psi_l \pm \Psi_k) \\ &= \sum_{k=1}^{\infty}\sum_{l=1}^{\infty} \hat{P_{kl}} \cdot \cos(r_{kl} x - \omega_{kl} t - \Psi_{kl})\,. \end{aligned} \tag{7}$$

with

$$\hat{P_{kl}} = \frac{\hat{B}_k \hat{B}_l}{2\mu_0}, \quad r_{kl} = \nu_l \pm \nu_k, \quad \omega_{kl} = \omega_l \pm \omega_k, \tag{8}$$

Force waves combine magnetic flux density waves two by two. As the wave numbers of the force waves are strongly related with the vibrational eigenmodes of the stator, they are also called mode numbers.

One common method to analyze magnetic force density waves is Jordan's combination table [1], by which the air gap field $b(x,t)$ is calculated from the permeance function of the machine and the magnetomotive forces (MMF). As shown in Table 1, the causes of typical air gap field harmonics can be derived. The wave numbers of harmonics excited by stator or rotor slotting, winding distribution or saturation are well known and described by the number of stator and rotor slot N_1 and N_2, the number of pole pairs p, the frequency of the fundamental component f_p. Simplifying assumptions and effects like saturation diminish the accuracy of quantitative statements concerning the amplitude of higher harmonics. In addition, it happens in practice that force density harmonics are obtained by FE analysis that were not identified by the analytical model.

III. Analysis of magnetic force density waves using numerical simulation data and a convolution approach

In comparison to the analytical approach, a two-dimensional electromagnetic FEM simulation provides an accurate representation of the magnetic flux density distribution. The air gap field can be sampled in time and space and the Fourier series coefficients can subsequently be approximated by means of the DFT. Since many air gap field waves combinations have the same wave number, a magnetic force density harmonic is usually the geometrical sum of a number of pairs of air gap field harmonics. The common approach of applying Fourier analysis to the force densities does not provide information about their composition. Before discussing the presented approach, the two-dimensional DFT and the usage of space vectors is briefly reviewed.

Table 1: Wave numbers and frequencies of typical air gap field harmonics.

Cause	Wave number ν	Frequency order ω/ω_0
Stator slotting	$gN_1 + p, g \in \mathbb{N}$	1
Rotor slotting (IM)	$gN_2 + p, g \in \mathbb{N}$	$1 + \frac{gN_2}{p} \cdot (1-s)$
Stator wind. distr.	$p(6g+1), g \in \mathbb{Z}$	1
Current harmonic μ	$p(6g+\mu), g \in \mathbb{Z}$	μ
Saturation	3p	3

A. Two-dimensional Fourier analysis

Say $T > 0, \omega = \frac{2\pi}{T}$ and $f : [0, 2\pi] \times [0, T] \to \mathbb{C}$ is a piecewise differentiable function. Then f can be represented by a Fourier series

$$f(x,t) = \sum_{n=-\infty}^{\infty}\sum_{m=-\infty}^{\infty} c_{nm} e^{j(nx+m\omega t)}\,. \tag{9}$$

The complex coefficients of the Fourier series are determined by

$$c_{nm} = \frac{1}{2\pi T}\int_0^{2\pi}\int_0^{T} f(x,t) e^{-j(nx+m\omega t)} dt dx\,. \tag{10}$$

The function f now be sampled at discrete locations in space

$$x_k = k\Delta x\,, \quad k \in \mathbb{Z}\,, \quad \Delta x > 0 \tag{11}$$

and discrete instants in time

$$t_l = l\Delta t\,, \quad l \in \mathbb{Z}\,, \quad \Delta t > 0\,. \tag{12}$$

If in addition, f is periodic in space and is sampled N times ($2\pi = N\Delta x$) and if it is also periodic in time with M sample points ($T = M\Delta t$, $\omega = \frac{2\pi}{T}$), then the function can be completely described by a matrix $Y \in \mathbb{C}^{N\times M}$. For the sake of simplicity $N, M \in \mathbb{N}$ be odd.

The two-dimensional discrete Fourier transform (2D-DFT), as approximation for the Fourier series of the function is defined as unique invertible linear mapping $\mathsf{2D\text{-}DFT} : Y \in \mathbb{C}^{N\times M} \to \bar{Y} \in \mathbb{C}^{N\times M}$ by means of the spectral coefficients

$$\bar{y}_{nm} = \frac{1}{NM}\sum_{k=0}^{N-1}\sum_{l=0}^{M-1} y_{kl} e^{-j(nx_k + m\omega t_l)}\,, \tag{13}$$

where y_{kl} are entries of the matrix $Y \in \mathbb{C}^{N\times M}$ and $\bar{y}_{nm}$ are entries of the matrix $\bar{Y} \in \mathbb{C}^{N\times M}$. The inverse mapping is called the two-dimensional inverse Fourier transform (2D-IDFT) and is defined by

$$y_{kl} = \sum_{n=0}^{N-1}\sum_{m=0}^{M-1} \bar{y}_{nm} e^{j(nx_k + m\omega t_l)}\,. \tag{14}$$

There are algorithms, such as the Fast Fourier Transform that efficiently compute (13) and (14).

The matrix Y approximates the function f, and $\bar{Y}$ its spectrum. If f is real, i.e. $y_{nm} \in \mathbb{R}\,\forall n, m$, then it can be written in the following form

$$f(x,t) \approx \sum_{n=0}^{N-1}\sum_{m=0}^{M-1} A_{nm} \cos(r_n x + m\omega t + \varphi_{nm})\,, \tag{15}$$

where $r_n = n - (N-1)/2$. This can be split into three parts:

$$\begin{aligned} f(x,t) \approx &\frac{a_{00}}{2} + \sum_{n=1}^{(N-1)/2} A_{n0} \cos(r_n x + \varphi_{n0}) \\ &+ \sum_{n=0}^{N-1}\sum_{m=1}^{(M-1)/2} A_{nm} \cos(r_n x + m\omega t + \varphi_{nm})\,, \end{aligned} \tag{16}$$

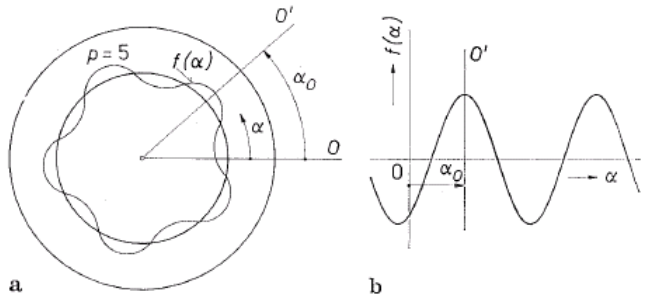

Figure 1: General illustrations of one-dimensional harmonic waves,(a) wave with p=5, (b) value along angle, from [8].

Therein, a_{00} corresponds to the DC component and zero order mode of the function f; A_{n0} are all DC components of the space harmonics. The remaining entries, e.g. $A_{nm}\,\forall m = 1\ldots(M-1)/2, n = 0\ldots N-1$, determine the time and space harmonic waves of f. Therefore, only the latter term of (16) is relevant for vibration analysis, as it can represent forward and backward traveling waves. Note that this double sum ranges from 1 to only $(M-1)/2$ which means, that the transformed matrix $\bar{Y}$ only contains half as much entries as Y. However, these entries are complex in contrast to the entries of Y, which have been assumed to be real. Practically, that means only positive frequencies, but positive and negative wave numbers r_n occur. Of course, the definition could also be chosen to have positive and negative frequencies and only positive wave number. The first convention is used in this paper.

B. Concept of space vectors

Space vectors are frequently used as a tool to describe and calculate the flux model of vector controlled electrical machines under various operation modes. However, space vectors offer also a more general description for arbitrary one-dimensional harmonic waves in electrical machines. A graphic definition of space vectors defined as complex numbers was first proposed for electrical machines by Kovács and Štěpina[8]. It allows a handling of harmonic waves in a convenient way. A single harmonic wave can be expressed by

$$\begin{aligned} f(\alpha) &= F_p \cdot \cos[p(\alpha-\alpha_0)+\omega(t-t_0)] \\ &= F_p \cdot Re\{e^{j(p\alpha_0+\omega t_0)}e^{-j(p\alpha+\omega t)}\}. \end{aligned} \tag{17}$$

The space vector is defined as the complex number

$$\underline{F} = F_p \cdot e^{j(p\alpha_0+\omega t_0)}. \tag{18}$$

In this way, the air gap field and magnetic force waves can be described by rotating vectors in the complex plane. The magnitude of the vector corresponds to the wave amplitude, whereas the angle corresponds to the phase shift as depicted in Figure 1.

C. Convolution approach

In the sampling procedure in space and time, a full period and a full revolution of the FEM solution data is stored into matrix B. In order to consider the magnetic force density waves, the magnetic force density matrix P is created by applying (5) to each matrix entry b_{kl}. Subsequently, a two-dimensional DFT of P provides the approximated Fourier series coefficient $\bar{p}_{nm}$. Path $(B, P, \bar{P})$ in Figure 2 illustrates this approach. The matrix $\bar{P}$ contains space vectors of harmonic magnetic force waves.

Path $(B, \bar{B}, \bar{P})$ in Figure 2 indicates an alternative way of calculating magnetic force density waves $\bar{P}$. First, the 2D DFT is applied directly to the air gap field matrix B. Then, $\bar{P}$ is obtained by matrix convolution. The two-dimensional periodic matrix convolution

$$Z = X * Y \tag{19}$$

of two given matrices $X, Y \in \mathbb{C}^{K\times L}$ is defined by

$$z_{st} = \sum_{k=0}^{K-1}\sum_{l=0}^{L-1} y_{kl}\cdot y_{(s-k)(t-l)}\,, \tag{20}$$

It is well known that a multiplication in time domain, e.g. B^2 corresponds to a convolution in frequency domain, e.g. $\bar{B} * \bar{B}$.

Applied to the air gap field DFT matrix, a periodic matrix convolution combines all matrix entries with each other:

$$\bar{P} = \frac{1}{2\mu_0}\cdot \bar{B} * \bar{B}. \tag{21}$$

This approach seems to be complex and costly. A complete convolution (20) would indeed be very time consuming. However, a complete convolution is not necessary since only a very small number of combination pairs do contribute significantly to the magnetic force density wave that really cause audible noise. Therefore, only the matrix entries of $\bar{b}_{nm}$, whose amplitude exceed a chosen threshold need to be considered in the calculation.

The advantage of this approach in contrast to path $(B, P, \bar{P})$, arises from the fact that each air gap field convolution pair is then known and can be stored. Thus, for each resulting force density wave $\bar{p}_{nm}$ a set of pairs

$$\bar{p}_{nm} : \{(\bar{b}_{n_1m_1}, \bar{b}_{n_2m_2}); (\bar{b}_{n_3m_3}, \bar{b}_{n_4m_4}); \ldots\} \tag{22}$$

is stored.

As an example result of such calculation, Table 2 shows the largest three contributions to the second order, mode four, excitation force density wave. The wave numbers and frequency orders must be added or subtracted to obtain $r = -4$ and $\omega/\omega_0 = 2$ according to (8).

D. Space vector diagram

Following the convolution approach $(B, \bar{B}, \bar{P})$, each magnetic force wave can be decomposed into the geometric addition of partial space vectors as shown in Figure 6 which represents the same data as Table 2. The depicted magnetic force density wave has mode number $r = -4$ and and a frequency order of $\omega/\omega_0 = 2$. Each of the partial vectors A, B, C is associated with an air gap field combination pair. The partial vectors are sorted according to their magnitude. The black line is the total magnetic force density vector calculated using path $(B, P, \bar{P})$. Obviously, the chain of partial vectors adds up to the total vector. A truncation error that depends on the chosen convolution threshold and on the number of stored partial vectors leads to a gap between the total vector and the vector chain.

IV. Numerical results

$$\begin{array}{ccc} B & \xrightarrow{\text{2D-DFT}} & \bar{B} \\ \downarrow \cdot & & \downarrow * \\ P & \xrightarrow{\text{2D-DFT}} & \bar{P} \end{array}$$

Figure 2: Commutative diagram.

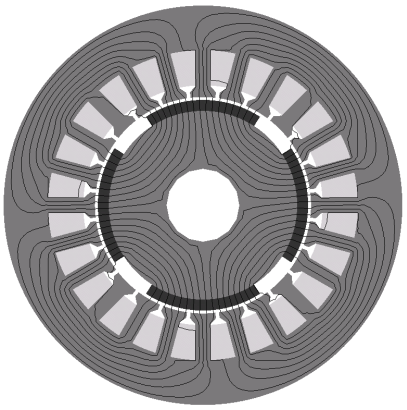

Figure 3: Stator and rotor of four pole example PMSM with field lines.

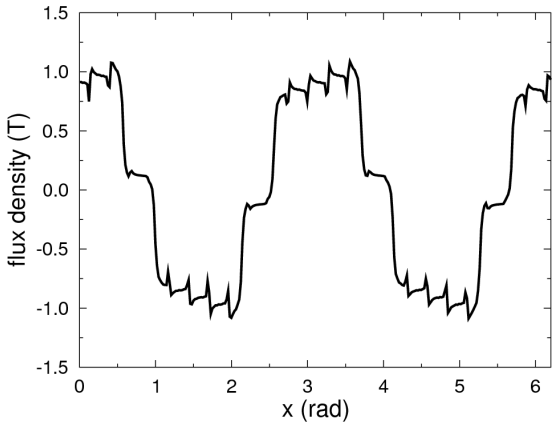

Figure 4: Radial air gap flux density.

A. Example machine

To demonstrate the proposed method, a permanent magnet excited synchronous machine (PMSM) is investigated. It is designed using in-house software for the automated sizing of PMSM [9]. Its cross-section together with the field distribution in rated operation can be seen from Figure 3.

The magnetic flux density is sampled in the air gap. This is done for each time step individually. The radial field for one time instance can be seen from Figure 4. The spectrum of the resulting force density waves are shown in Figure 5. The combination of the fundamental field with it self typically yields high amplitudes, in this case it is 162775 N/m^2. The scale of Figure 5, however, was chosen to clearly depict the most relevant higher force density harmonics of modes r=0,2 and 4 and only

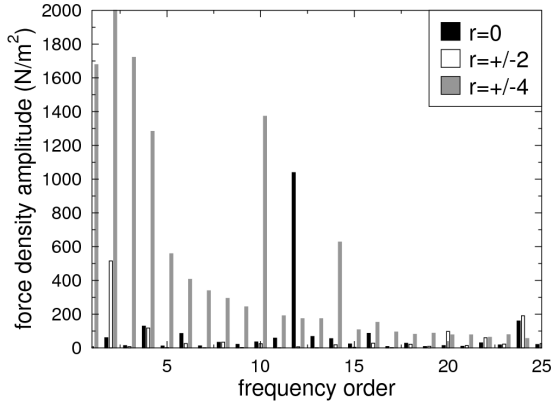

Figure 5: Force density amplitude of different modes.

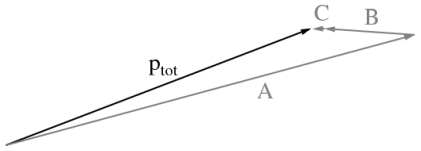

Figure 6: Space vector diagram for $r = -4$ and $\omega/\omega_0 = 2$.

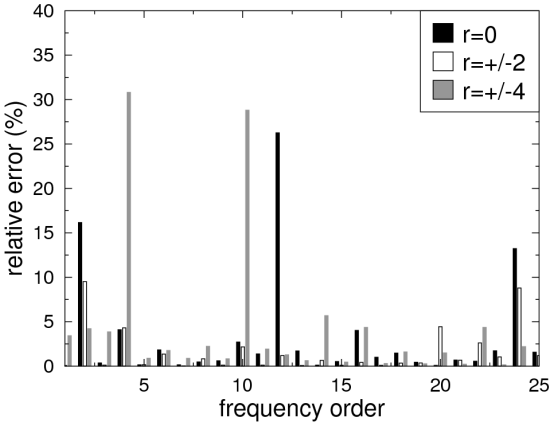

Figure 7: Deviation between MST and $B^2/2\mu_0$.

the maximum amplitude of the positive and negative modes is shown.

The convolution approach is applied to the air gap field sampled in time and space. As a first example, the second order, mode 4 force density harmonic, which is supposed to be excited by the fundamental field convoluted by itself, is analyzed. All flux density waves that are larger than 0.01% of the fundamental field are considered as convolution partners. The space vector diagram of Figure 6 shows the three most relevant partial space vectors. Their wave numbers and orders are given in Table 2. The fundamental field squared (A) adds by far the largest contribution, however, at least one more flux density wave combination (B) shows a minor influence.

B. Comparison with full stress tensor calculation

To justify the approach and to investigate its limits, the force density in mode/frequency domain obtained from stress tensor using (1), which would be typically used for a subsequent structural dynamic simulation, is compared to the simplified formula (5). Figure 7 shows the relative deviation between those two. For the fundamental field square, its magnitude is used as reference value, for all other waves, 2000 N/m^2 is used as reference value, which corresponds to the maximum amplitude shown in Figure 5. The deviation of the angle between the calculation using (1) and (5) is shown in Figure 8 for all waves with an amplitude larger than 600 N/m^2, which is less than 0.5% of the amplitude of the fundamental field squared. It can be seen that the relative error is below 40% and the angle error is less than 30^o for all shown harmonics. The deviation is still significant

Table 2: Contributing air gap fields.

$r = -4; \quad \omega/\omega_0 = 2$
$p_{tot} = 170258\,\mathrm{N/m^2} < 21^o$

Space vector	ω/ω_0	ν	ω/ω_0	ν
A	1	-2	1	-2
B	1	-2	3	-6
C	5	-10	7	-14

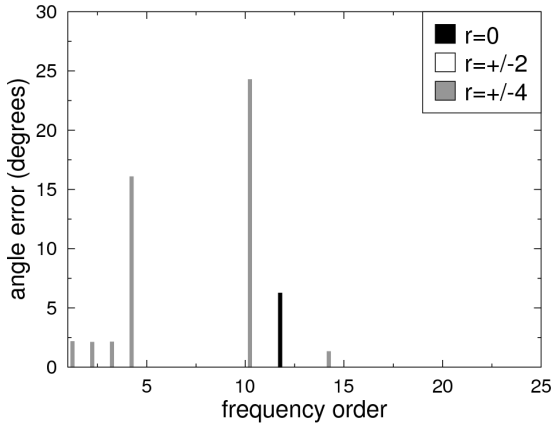

Figure 8: Deviation between MST and $B^2/2\mu_0$.

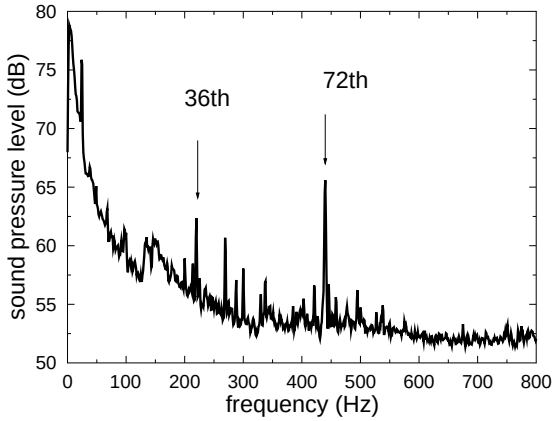

Figure 9: Measured sound pressure level.

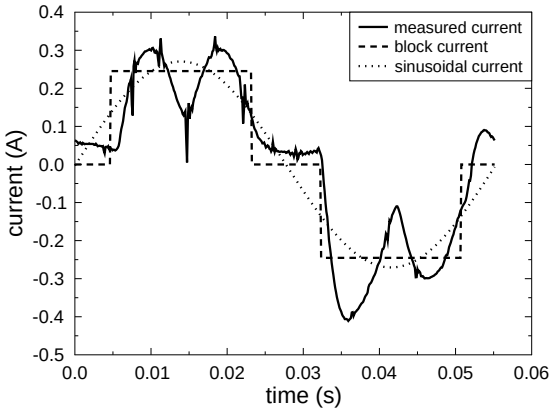

Figure 10: Comparison of current waveforms.

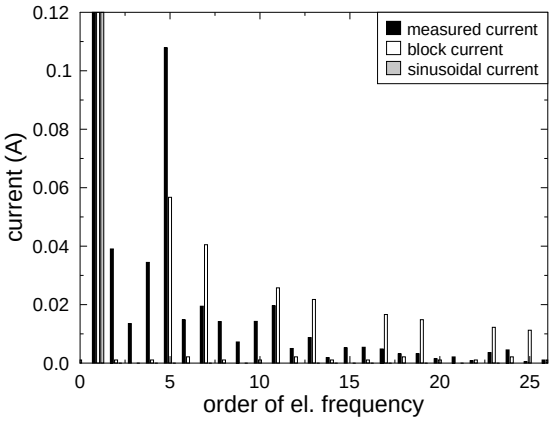

Figure 11: Spectral comparison of current (fundamental of approx. 0.3A not shown).

as to still use the full stress tensor calculation for the excitation of precise structural dynamic simulations, however, the obtained accuracy can be considered sufficient for studying the contributions of the individual flux density waves to a particular force wave.

V. Application

A. Brushless DC motor drive

The BLDC motor under analysis is a 500 W, six pole machine with nine stator slots designed as a variable speed drive.

Laboratory tests evidented disturbing audible single tones at some speeds, which are most probably due to resonances of mode zero of the supporting mechanical structure. Fig 9 shows airborne sound for n=367 1/min. The 36^{th} and 72^{th} order of mechanical speed can be clearly identified as disturbing single tones. By means of analytical approach [10], it is possible to show that current time harmonics are involved in the generation of these frequencies. It however, does not provide any quantitative statement about the influence of the current harmonics on the magnetic force.

For cost reasons, the BLDC is not equipped with a feedback current control loop, which would require accurate current sensing. Therefore, the BLDC is operated in open loop voltage control. This leads to additional current harmonics when compared to a pure rectangular current waveform. So the question is, whether the additional current harmonics are the reason for the disturbing noise. There are three options which are considered for the current excitation: Pure sine wave current, e.g. by means of a PWM converter, a pure rectangular current waveform and the measured current resulting from the open loop voltage supply. For n=367 1/min, the current waveforms and spectra are shown in Figure 10 and 11, respectively.

Applying 2D FEM analysis to this problem yields the force excitation modal distribution. It shows that for the 36^{th} order the measured current actually represents the best option in terms of force excitation. For the 72^{th} order, sinusoidal supply current is clearly the best choice. It remains the question, why does the open loop voltage supply lead to less noise for the 36^{th} order and why does the rectangular current supply give so large force excitations.

Applying the proposed convolution approach the space vector diagrams in Figure 12 and 13 are obtained for measured currents and sinusoidal current supply, respectively. For the 36^{th} order, it can be seen that the individual force contributions only very slightly between the two excitation types, however the phase angle varies significantly and result in a lower total force for the measured current excitation. The sensitivity of force excitation to current harmonics together with the possibility to precisely study their influence allows for an optimization of current with respect to noise, which however is not subject here. For the 72^{th} order, the resulting space vector data are given in Figure 14 and 15 for measured currents and block currents, respectively. It can be seen that the most significant contributions to the force excitation with the measured currents are the 416 Hz and 453 Hz components with $\nu = 3 = p$.

From Table 1, it can be seen that these can only stem from stator current harmonics of $\mu = 23$ and 25, respectively. The space vector diagram shows that for the case with measured currents, vector A and and B are in perpendicular, where they are

f = 217 Hz
r = 0
p_{tot} = 636 N/m^2 < -172^o

Vector	f1,nu1	f2,nu2
A	18Hz,33	199Hz,-33
B	18Hz,-3	199Hz,3
C	54Hz,27	163Hz,-27
D	18Hz,-3	235Hz,-3
E	54Hz,-9	163Hz,9
F	18Hz,-39	235Hz -39

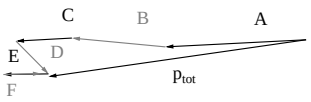

Figure 12: Space vector diagram with measured currents at 36$^{\text{th}}$ order of mechanical speed.

f = 217 Hz
r = 0
p_{tot} = 836 N/m^2 < -175^o

Vector	f1,nu1	f2,nu2
A	18Hz,-3	199Hz,3
B	18Hz,33	199Hz,-33
C	54Hz,27	163Hz,-27
D	54Hz,-9	163Hz,9
E	18Hz,-39	235Hz,-39
F	18Hz,-3	235Hz,-3

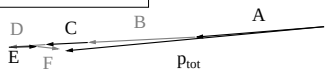

Figure 13: Space vector diagram with sinusoidal currents at 36$^{\text{th}}$ order of mechanical speed.

f = 434 Hz
r = 0
p_{tot} = 36 N/m^2 < -76^o

Vector	f1,nu1	f2,nu2
A	18Hz,-3	416Hz,3
B	18Hz,-3	453Hz,-3
C	18Hz,-75	453Hz,-75
D	18Hz,69	416Hz,-69
E	54Hz,-9	380Hz,9
F	127Hz,51	308Hz,-51

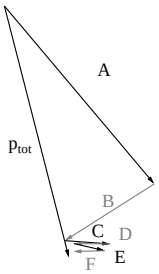

Figure 14: Space vector diagram with measured currents 72$^{\text{th}}$ order of mechanical speed.

f = 434 Hz
r = 0
p_{tot} = 226 N/m^2 < 78^o

Vector	f1,nu1	f2,nu2
A	18Hz,-3	416Hz,3
B	18Hz,-3	453Hz,-3
C	54Hz,-9	380Hz,9
D	18Hz,-75	453Hz,-75
E	18Hz,69	416Hz,-69
F	127Hz,51	308Hz,-51

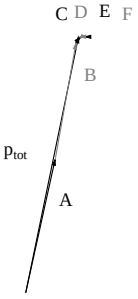

Figure 15: Space vector diagram with block currents 72$^{\text{th}}$ order of mechanical speed.

much larger and in phase in case of rectangular currents. This is confirmed by the current spectrum Figure 11, as the measured current has much lower harmonic components for $\mu = 23$ and 25 than the block current.

The analysis showed that the single tones are not due to, but in fact are even lower, for the open loop voltage supply compared to a close loop current regulation.

B. IPMSM

The developed convolution and space vector approach is applied to the vibration problem of an interior permanent magnet synchronous machine (IPMSM) with eight magnets and 18 stator slots. As it is used over a wide speed range with limited supply voltage, field-weakening operation is required. On the test bench, it is found that the supply voltage and therefore the degree of field-weakening has a significant influence on the acoustic behavior of the machine.

In base speed operation, current leads the d-axis by an angle of 90^o. For field-weakening, a demagnetization is required and can be achieved by the current leading the d-axis by an angle more than 90^o. The angle between current and the q-axis is defined as

$$\gamma = \beta - \frac{\pi}{2}\,, \tag{23}$$

where β is the angle between current and the d-axis [11]. In this case, for base speed operation, $\gamma = 25^o$, and for field-weakening $\gamma > 25^0$, since reluctance, which is due to saliency, is utilized.

The field distribution in the machine is computed using FE simulation for different speeds above base speed. The Fourier decomposition of the electromagnetic forces shows that the important orders of mechanical frequency strongly depend on γ. For the 8^{th} and 16^{th} order, the force excitation with critical modes numbers decrease with γ. The force excitations of 24^{th} and 48^{th} order increase with γ, however these excitations are in most cases not critical, since they are excited with mode number 6, which is comparatively large. For the 32^{th} and 56^{th} order, the force excitation is strongly increased for mode 8, slightly increased for mode 2 and decreased for mode 4 with γ.

For the analysis of this behavior, the convolution approach is applied and results are shown in Figure 16 and in Table 3 exemplary for $r = 2$ and the 16^{th} order of mechanical frequency for different values of γ.

The magnitude of force waves, to which the fundamental field component contributes, are reduced with increasing γ. This can be seen, e.g. from lines 1, 8, 13 and 18 in Table 3, where the magnitude of the force wave decreases from $8109\frac{\text{N}}{\text{m}^2}$ to $3145\frac{\text{N}}{\text{m}^2}$. Excitations, in which the fundamental field component is not involved, vary slightly, possibly due to less saturation for increasing field-weakening, see e.g. lines 2,6,11 and 16. However, it can be said that the reduction of the fundamental field dominates the force excitation and therefore the total force excitation decreases with increasing to γ. It shows that the decomposition of force excitations by means of the proposed approach also yields more insight into the generation process of force waves for the field weakening of IPMSM.

VI. Summary and Conclusions

The approach presented in this paper allows the determination of the contributions of partial force density waves to specific force density waves. The approach is based on the 2D Fourier transform representation of the magnetic flux density in the air gap and its convolution with itself. It is shown that the convolution can be limited to the computation of the most relevant matrix

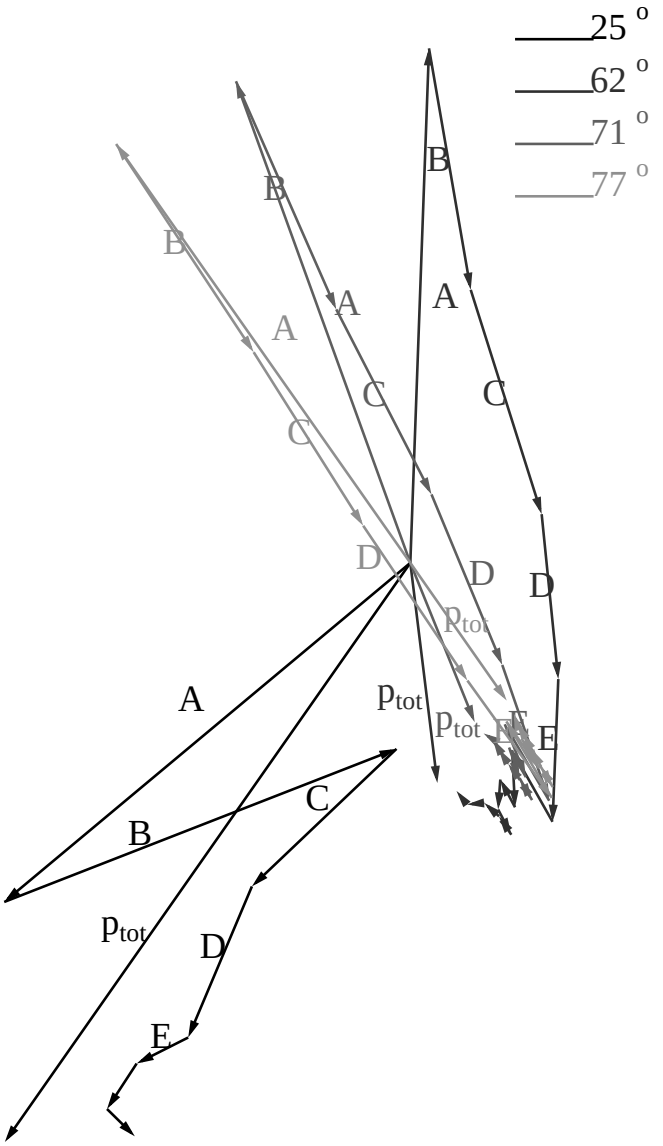

Figure 16: Space vector diagram of force excitation for different values of γ for $r = 2$ and 16^{th} order.

Table 3: Force density excitation space vectors for $r = 2$ and 16^{th} order.

γ	No.	Vec.	$\hat{p_k}\left(\frac{\text{N}}{\text{m}^2}\right)$	φ_k	ν_1	ord.	ν_2	ord.
25^o	1	A	8109	-140^o	4	4	-6	12
	2	B	6454	21^o	-14	4	12	12
	3	C	3058	-136^o	4	4	2	20
	4	D	2513	-113^o	22	4	20	20
	5	E	885	-153^o	-32	4	30	12
62^o	6	A	7891	88^o	-14	4	12	12
	7	B	3756	-80^o	22	4	20	20
	8	C	3606	-72^o	4	4	-6	12
	9	D	2540	-84^o	12	12	10	28
	10	E	2189	-92^o	4	4	2	20
71^o	11	A	7850	110^o	-14	4	12	12
	12	B	3819	-66^o	22	4	20	20
	13	C	3189	-63^o	4	4	-6	12
	14	D	2831	-67^o	12	12	10	28
	15	E	2201	-71^o	4	4	2	20
77^o	16	A	7845	125^o	-14	4	12	12
	17	B	3824	-57^o	22	4	20	20
	18	C	3145	-58^o	4	4	-6	12
	19	D	2860	-56^o	12	12	10	28
	20	E	2215	-54^o	4	4	2	20

entries. As an example, the air gap field and the force density waves of a PMSM are analyzed to demonstrate the effectiveness of the proposed approach. For this example, the error between the full stress tensor calculation and its simplified version is analyzed. The error is not negligible, but is still small enough to apply the proposed approach in noise and vibration diagnosis of electrical machines. As practical application a brushless DC motor drive and an IPMSM are analyzed.

VII. References

[1] H. Jordan, *Geräuscharme Elektromotoren*, H. Franz, Ed. W. Girardet, November 1950.

[2] J. Gieras, C. Wang, and J. C. Lai, *Noise of Polyphase Electric Motors*. CRC Press Taylor&Francis Group, 2006.

[3] M. Furlan, A. Cernigoj, and M. Boltezar, "A coupled electromagnetic-mechanical-acoustic model of a dc electric motor," *COMPEL: The International Journal for Computation and Mathematics in Electrical and Electronic Engineering*, vol. 22, no. 4, pp. 1155–1165, 2003.

[4] C. Schlensok, B. Schmülling, M. van der Giet, and K. Hameyer, "Electromagnetically excited audible noise evaluation and optimization of electrical machines by numerical simulation," *COMPEL: The International Journal for Computation and Mathematics in Electrical and Electronic Engineering*, vol. 26, pp. 727 – 742, 2007.

[5] T. Kobayashi, F. Tajima, M. Ito, and S. Shibukawa, "Effects of slot combination on acoustic noise from induction motors," *Magnetics, IEEE Transactions on*, vol. 33, no. 2, pp. 2101–2104, 1997.

[6] F. Henrotte and K. Hameyer, "A theory for electromagnetic force formulas in continuous media," *Magnetics, IEEE Transactions on*, vol. 43, no. 4, pp. 1445–1448, April 2007.

[7] J. Melcher, *Continuum Electromechanics*. MIT Press Cambridge Massachusetts, 1981.

[8] J. Štěpina, "Komplexe Größen in der Elektrotechnik," *Electrical Engineering (Archiv für Elektrotechnik)*, vol. 72, no. 6, pp. 407–414, November 1989.

[9] M. Hafner, M. Schöning, and K. Hameyer, "Automated sizing of permanent magnet synchronous machines with respect to electromagnetic and thermal aspects," in *Proceedings of the 2008 International Conference on Electrical Machines*, 2008.

[10] Z. Zhu and D. Howe, "Electromagnetic noise radiated by brushless permanent magnet dc drives," in *Electrical Machines and Drives, 1993. Sixth International Conference on (Conf. Publ. No. 376)*, 1993, pp. 606–611.

[11] T. J. E. Miller, *Brushless Permanent-Magnet and Reluctance Motor Drives (Monographs in Electrical and Electronic Engineering)*. Oxford University Press, USA, 6 1989.

Authors name and Affiliation

Michael van der Giet, Richard Rothe,
Mercedes Herranz Gracia and Kay Hameyer
Institute of Electrical Machines
RWTH Aachen University
Schinkelstrasse 4
D-52056 Aachen, Germany